Article

Observation of a linked-loop quantum state in a topological magnet

Ilya Belopolski[1,2,13 ✉], Guoqing Chang[3,13], Tyler A. Cochran[1,13], Zi-Jia Cheng[1,13], Xian P. Yang[1], Cole Hugelmeyer[4], Kaustuv Manna[5,6], Jia-Xin Yin[1], Guangming Cheng[7], Daniel Multer[1], Maksim Litskevich[1], Nana Shumiya[1], Songtian S. Zhang[1], Chandra Shekhar[5], Niels B. M. Schröter[8], Alla Chikina[8], Craig Polley[9], Balasubramanian Thiagarajan[9], Mats Leandersson[9], Johan Adell[9], Shin-Ming Huang[10], Nan Yao[7], Vladimir N. Strocov[8], Claudia Felser[5] & M. Zahid Hasan[1,7,11,12 ✉]

Quantum phases can be classified by topological invariants, which take on discrete values capturing global information about the quantum state[1–13]. Over the past decades, these invariants have come to play a central role in describing matter, providing the foundation for understanding superfluids[5], magnets[6,7], the quantum Hall effect[3,8], topological insulators[9,10], Weyl semimetals[11–13] and other phenomena. Here we report an unusual linking-number (knot theory) invariant associated with loops of electronic band crossings in a mirror-symmetric ferromagnet[14–20]. Using state-of-the-art spectroscopic methods, we directly observe three intertwined degeneracy loops in the material's three-torus, T^3, bulk Brillouin zone. We find that each loop links each other loop twice. Through systematic spectroscopic investigation of this linked-loop quantum state, we explicitly draw its link diagram and conclude, in analogy with knot theory, that it exhibits the linking number (2, 2, 2), providing a direct determination of the invariant structure from the experimental data. We further predict and observe, on the surface of our samples, Seifert boundary states protected by the bulk linked loops, suggestive of a remarkable Seifert bulk–boundary correspondence. Our observation of a quantum loop link motivates the application of knot theory to the exploration of magnetic and superconducting quantum matter.

Quantum topology is powerful in understanding condensed-matter systems that exhibit a winding[1–13]. Often, this winding occurs in real space. For example, in a magnetic material, the local magnetization may exhibit a rotating pattern centred around a point in real space, forming a magnetic vortex encoding an integer winding number[2,6]. Alternatively, the winding may occur in momentum space. For example, in a one-dimensional topological insulator, the quantum-mechanical wavefunctions wind as the momentum scans through the Brillouin zone[3,4,8–13]. These two broad paradigms— order parameters, such as magnetization, that wind in real space and quantum wavefunctions that wind in momentum space—capture a vast landscape of topological phases of matter, spanning decades of research by myriad communities of physicists. Despite their importance in modern physics, there is no indication that these two paradigms are exhaustive. New paradigms for topology promise to deepen our fundamental understanding of nature, as well as enable new quantum technologies.

Recently, there has been considerable interest in node loops, electronic structures in which multiplebands cross along a closed curve in momentum space[13–15,21–25]. Away from the crossing curve, the bands disperse linearly, so that the node loop consists of a cone dispersion persisting along a loop. Within the paradigm of momentum-space wavefunction winding, node loops are topological, with a quantized-Berry-phase invariant[9,10,13,24,25]. However, in contrast to other electronic structures studied so far[8–13], node loops can link each other, encoding a linking-number invariant (Fig. 1a and Extended Data Fig. 1)[16–20]. Unlike the traditional paradigms of winding, this linking number is associated with the composite loop structure of quantum-mechanical band crossings of the Hamiltonian. Such linked node loops offer the possibility of a new bridge between physics and knot theory. It has further been proposed that these links are governed by emergent non-Abelian node-loop charges[16] and that the linking number determines the θ angle of the axion Lagrangian in certain node-loop phases[19,26,27]. As the three-dimensional condensed-matter
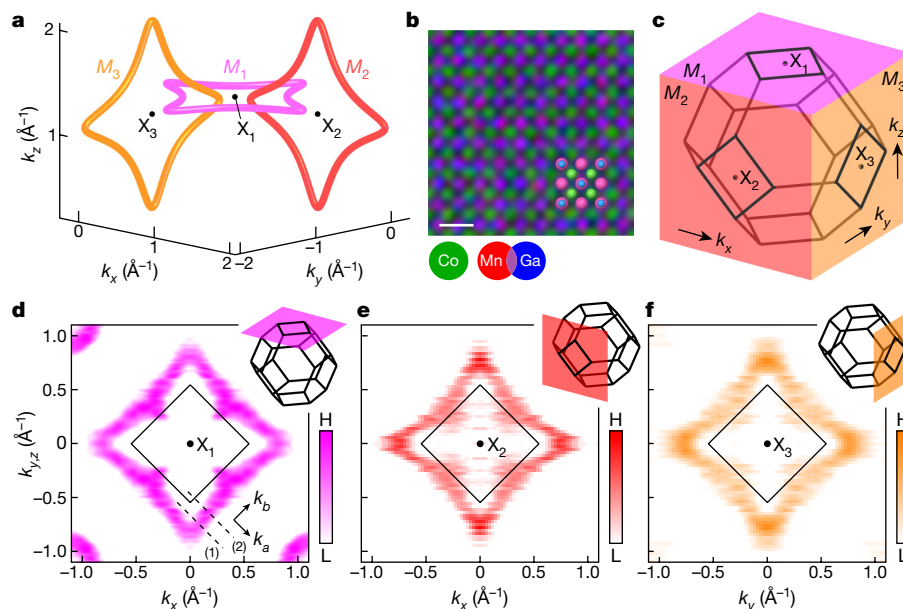
Fig. 1 | Signatures of linked node loops in Co$_2$MnGa. a, Weyl loops in the electronic structure of Co$_2$MnGa, predicted by DFT. Three distinct Weyl loops are confined to the three mirror planes M_1, M_2 and M_3, in such a way that the loops link one another (further copies of the loops in higher Brillouin zones not shown). **b**, Element-resolved crystal structure of Co$_2$MnGa along the [001] direction, acquired by atomic-level EDS. Atomic columns consist either entirely of cobalt (green) or of alternating manganese (red) and gallium (blue). Scale bar, 5 Å. **c**, Bulk Brillouin zone (black truncated octahedron) of Co$_2$MnGa with three mirror planes indicated, M_1 (magenta, constant k_z), M_2 (red, constant k_y) and M_3 (gold, constant k_x). Each mirror plane contains square faces of the Brillouin zone. The high-symmetry momentum-space points at the centre of each square are marked X_1, X_2 and X_3. **d**, Fermi surface acquired by ARPES at incident photon energy 544 eV, corresponding to M_1. H, L, high, low photoemission intensity. Dashed lines mark the energy–momentum slices shown in Fig. 2a. Inset: the M_1 mirror plane plotted in an extended bulk Brillouin zone scheme. **e**, Out-of-plane Fermi surface acquired on the same Co$_2$MnGa sample by an ARPES photon-energy dependence from 500 eV to 800 eV in steps of 2 eV, corresponding to M_2. **f**, Analogous out-of-plane Fermi surface corresponding to M_3, again on the same sample.

Brillouin zone is a three-torus (T^3), linked node loops also offer the rare possibility of observing links in a space other than ordinary infinite space (R^3). Moreover, the Seifert surface of the bulk link is associated with topological boundary states, opening the possibility of a unique Seifert bulk–boundary correspondence in quantum matter[28–32].

Ferromagnets with crystalline mirror symmetry naturally give rise to node loops. In this scenario, the ferromagnetic exchange interaction produces spin-split electronic bands that are generically singly degenerate throughout momentum space, and mirror symmetry protects two-fold band degeneracies along closed curves confined to the momentum-space mirror planes[22]. Such node loops are called Weyl loops, by analogy with the two-fold degeneracy of a Weyl point[11,12,23–25]. Weyl loops are effective at concentrating Berry curvature, giving rise to giant anomalous Hall and Nernst effects, up to room temperature and promising for technological applications[14,33–37]. In crystallographic space groups with multiple perpendicular mirror planes, different Weyl loops living in different mirror planes can naturally link each other[15,20]. The ferromagnet Co$_2$MnGa exhibits a crystal structure with multiple perpendicular mirror planes and was recently observed to host electronic Weyl loops[14,15], bringing together the key ingredients for linked node loops.

Linked Weyl loops

Co$_2$MnGa crystallizes in the full Heusler structure, with a face-centred cubic Bravais lattice, space group $Fm\bar{3}m$ (number 225), octahedral point group O_h and Curie temperature T_C = 690 K (Fig. 1b and Extended Data Fig. 2). The point group includes mirror planes normal to $\hat{x}$, $\hat{y}$ and $\hat{z}$ (conventional unit-cell lattice vectors). The real-space mirror planes give rise to momentum-space mirror planes, labelled M_1 (normal to $\hat{z}$), M_2 ($\hat{y}$) and M_3 ($\hat{x}$; Fig. 1c). Motivated by the observation of mirror-symmetry-protected magnetic Weyl loops in Co$_2$MnGa (refs. [14,15]), we explore the electronic structure of our samples on M_1, M_2 and M_3. We perform ab initio calculations of Co$_2$MnGa in the ferromagnetic state, focusing on these three mutually perpendicular mirror planes. We find that each mirror plane hosts a Weyl loop, and that the three Weyl loops link one another (Fig. 1c). To experimentally investigate this ab initio prediction, we carry out angle-resolved photoemission spectroscopy (ARPES) using soft X-ray photons, optimized for exploring bulk electronic states[38,39]. To simplify the presentation of our results, we first discuss the Weyl loops one at a time (Figs. 1 and 2), then consider their linking two at a time (Fig. 3) and finally consider the full three-component link (Fig. 4). We first acquire a Fermi surface at a fixed incident photon energy $h\nu$ = 544 eV, chosen to fix the k_z momentum near this 'in-plane' mirror plane (M_1; Fig. 1d and Supplementary Section 1). We observe a diamond-shaped contour centred on X_1, which traces out a momentum-space trajectory encircling the square top face of the bulk Brillouin zone. We also observe a small circular feature at the corners of the Fermi surface, which arises from an unrelated band at Γ, irrelevant for what follows. We next perform a photon-energy dependence on the same sample, measuring from $h\nu$ = 500 to 800 eV, which allows us to access the electronic structure on the 'out-of-plane' mirror M_2 (Fig. 1e). We again observe a diamond-shaped loop contour, now centred on X_2 and encircling the square side face of the bulk Brillouin zone. We then rotate the sample by 90° and repeat the same photon-energy dependence to capture the electronic structure on the other 'out-of-plane' mirror M_3. We observe again a similar diamond-shaped loop contour centred on X_3 (Fig. 1f). These systematic observations suggest a family of diamond-shaped loop contours, each living in one of the three mirror planes.

To further understand the loop electronic structures, we examine energy–momentum photoemission spectra slicing through the M_1 loop
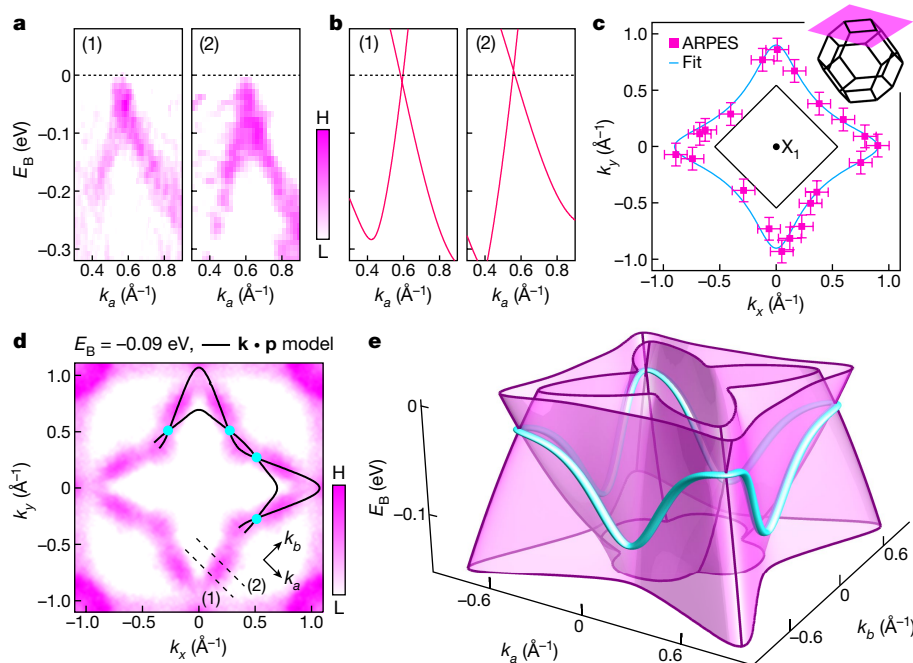
Fig. 2 | Weyl loop trajectory in Co₂MnGa. a, Energy–momentum photoemission slices through the loop Fermi surface (slice locations marked by the dashed lines in **d** and Fig. 1d). **b**, Energy–momentum slices through the Weyl loop from DFT, showing a Weyl loop cone (slice locations marked in Extended Data Fig. 3c). **c**, Cone locations (magenta squares) systematically extracted from cone dispersions observed in photoemission spectra on M_1. Error bars indicate the experimental resolution. Experimental loop trajectory extracted by fitting to the cone locations (cyan; see text). The binding energy axis is collapsed. **d**, Constant-energy photoemission slice with the analytical model of the Weyl loop (black lines). This slice intersects the Weyl loop at a discrete set of points (cyan dots). **e**, Dispersion of an effective $\mathbf{k}\cdot\mathbf{p}$ Hamiltonian for the Weyl loop, obtained by fitting to the ARPES spectra. In **a** and **d**, H, L, high, low photoemission intensity.

(Fig. 2a). We observe two bands that disperse towards each other and meet near the Fermi level, E_F (binding energy $E_B = 0$), suggesting a cone dispersion persisting in momentum space and tracing out the M_1-loop Fermi surface. As Co₂MnGa is ferromagnetic, we expect generically singly degenerate bands throughout the Brillouin zone. This suggests a cone dispersion consisting of singly degenerate branches that exhibit a double degeneracy at the touching points, indicating a Weyl loop electronic structure. The corresponding ab initio calculations also show a Weyl cone with characteristic two-fold degenerate crossing and linear dispersion, in good agreement with the ARPES data (Fig. 2b). To further characterize the Weyl loop experimentally, we systematically track all cone crossings observed along the full M_1-loop trajectory (Fig. 2c and Extended Data Fig. 3) and also examine a deeper constant-energy photoemission slice through the Weyl loop (Fig. 2d). We then quantitatively capture the experimental dispersion by fitting the data to a minimal two-band effective $\mathbf{k}\cdot\mathbf{p}$ Hamiltonian for a Weyl loop, with all parameters extracted directly from the photoemission spectra (Fig. 2e and Methods). The extracted dispersion reaches the Fermi level within experimental resolution, suggesting that the observed Weyl loops are relevant for low-energy response and consistent with previous reports that Weyl loops play a dominant role in the giant anomalous Hall effect and other exotic transport properties of Co₂MnGa (refs. [14,34–36]). Our photoemission spectra, ab initio calculations and $\mathbf{k}\cdot\mathbf{p}$ model suggest that we have observed a magnetic Weyl loop on M_1.

We next investigate the composite structure formed by pairs of Weyl loops, focusing on the Weyl loop crossing itself (degeneracy curve, shown in cyan in Fig. 2e). The loop crossing disperses in energy, so a constant-energy slice through the electronic structure typically intersects a loop crossing only at several discrete points (for example, the cyan dots in Fig. 2d). However, despite this energy dispersion, we find
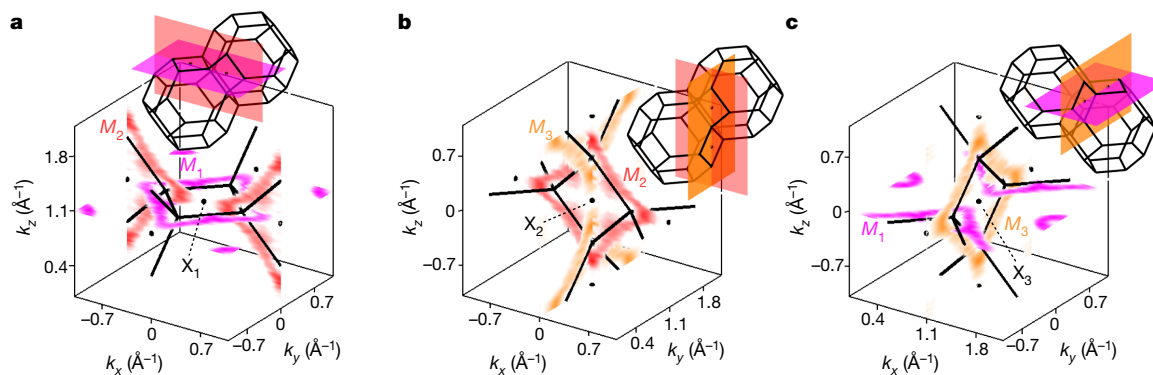

Fig. 3 | Linked Weyl loops in Co₂MnGa. a, M_1- and M_2-loop Fermi surfaces plotted in adjacent bulk Brillouin zones, exhibiting a link structure. Inset: M_1 and M_2 plotted across multiple Brillouin zones. **b**,**c**, As for **a**, but for the M_2- and M_3-loop Fermi surfaces (**b**) and the M_3- and M_1-loop Fermi surfaces (**c**). The momentum axes are shifted by reciprocal lattice vectors to present the datasets in the vicinity of the first bulk Brillouin zone (Extended Data Fig. 10).
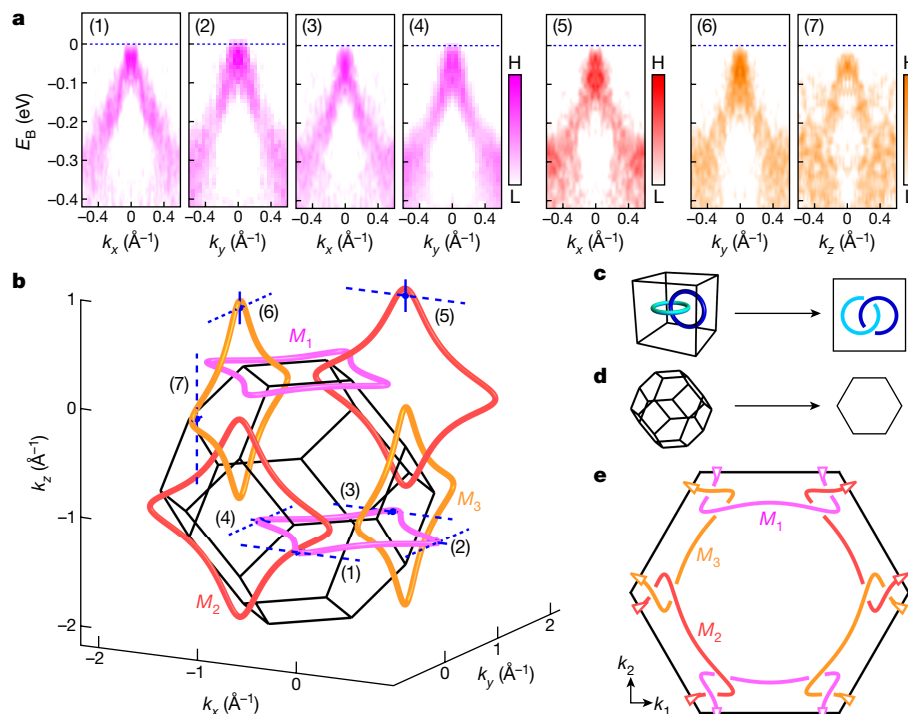
Fig. 4 | Linking number (2, 2, 2) in topological quantum matter. a, Energy–momentum photoemission slices tangential to the M_1, M_2 and M_3 Weyl loops at their extrema. H, L, high, low photoemission intensity. **b**, Weyl loops from adjacent bulk Brillouin zones, exhibiting links. The loop trajectories are obtained by fitting equation (2) to the ARPES spectra (as detailed in Fig. 2) and then applying the symmetries of the lattice to obtain all three loops. The Weyl cone positions (blue dots) are extracted from the slices in **a** (dashed blue lines), consistent with the analytical model (short blue line segments indicate the error). **c**, Link diagrams help visualize a three-dimensional link structure by flattening it to two dimensions while retaining the link information, illustrated

for the example of a Hopf link. **d**, In a crystal, it is natural to draw link diagrams in the surface Brillouin zone, such as the (111) surface Brillouin zone (hexagon, Extended Data Fig. 2). **e**, Link diagram for the Co_2MnGa linked Weyl loops. There are three distinct Weyl loops and each loop links each other loop exactly twice, giving the geometric linking number (2, 2, 2). The arrows indicate out-of-plane wrapping: as one follows the loop in the direction of the arrow, the loop wraps out of the page, exiting the Brillouin zone from the front and re-entering from the back, at the same time reconnecting at the opposite edge of the hexagon.

that the typical 'radius' of the Weyl loop, $|k|_{avg} = 0.66$ Å^{-1}, is much larger than the typical momentum separation of the two branches of the Weyl cone at the Fermi level, $\eta/v_F = 0.07$ Å^{-1}, where η sets a typical energy scale and v_F is the Fermi velocity (Methods). As $|k|_{avg} \gg \eta/v_F$, we can treat the Weyl loop crossing as approximately flat in energy, and we can accurately capture its trajectory by examining a constant-energy slice near the Fermi level. Therefore, to understand the composite structure of the Weyl loops, we can focus on the M_1-, M_2- and M_3-Weyl-loop Fermi surfaces. We first consider the M_1 and M_2 Weyl loops and zoom in on the momentum-space region around X_1 (Fig. 3a, inset). By plotting the M_1- and M_2-Weyl-loop Fermi surfaces simultaneously in this region of three-dimensional momentum space, we observe that these two loops seem to link each other twice (Fig. 3a). Repeating the analogous procedure for X_2 and X_3, we observe that the M_2 and M_3 Weyl loops also link twice (Fig. 3b), and similarly for the M_3 and M_1 Weyl loops (Fig. 3c). Our three-dimensional momentum-space analysis of the photoemission spectra suggests that each of the M_1, M_2 and M_3 Weyl loops links each other loop twice, forming an interwoven structure (Extended Data Figs. 4 and 5).

Link diagram in the Brillouin zone

To further explore this link, we examine all three Weyl loops simultaneously using the experimentally extracted loop trajectory (Methods and equation (2)). In an extended zone scheme, we plot the M_1, M_2 and M_3 Weyl loops around six nearby X points, so that two redundant copies of each Weyl loop are included (Fig. 4b). We find that the three Weyl loops all link together, forming a single composite linked structure.

To further characterize the links, we examine energy–momentum photoemission slices tangential to all three loops near their extrema (Fig. 4a and Extended Data Figs. 6–8). All slices exhibit a cone dispersion, consistent with the Weyl loop electronic structure. Moreover, we find quantitative agreement between the Weyl loop extrema expected from equation (2) and the locations of the photoemission cone dispersions, for all three loops.

To better characterize the complete link structure, we construct a link diagram for our Weyl loops. In such a link diagram, we flatten the link from three to two dimensions while preserving the link information using an over/under notation (illustrated for the example of a Hopf link; Fig. 4c). As the Weyl loop link lives in the periodic momentum space of the crystal, it is necessary and sufficient to consider all link components in a single Brillouin zone. To draw a link diagram, we therefore flatten the link into the surface Brillouin zone. Moreover, because our analysis shows that all three Weyl loops are symmetry related, we choose the (111) surface Brillouin zone (Extended Data Fig. 2), which treats X_1, X_2 and X_3 equivalently (Fig. 4d). The resulting link diagram uniquely specifies the Co_2MnGa quantum link and shows three loops straddling the edges of the surface Brillouin zone (Fig. 4e and Supplementary Section 4). We observe that the link wraps around T^3 in all three momentum-space directions. This behaviour suggests that the link is geometrically essential, so that it cannot be smoothly perturbed to live entirely within a local region of the Brillouin zone. The link diagram further shows that each loop is linked with each other loop exactly twice. This gives 2 for the geometric linking number, defined as the minimal number of crossing changes between link components needed to separate the components. The geometric linking number of the
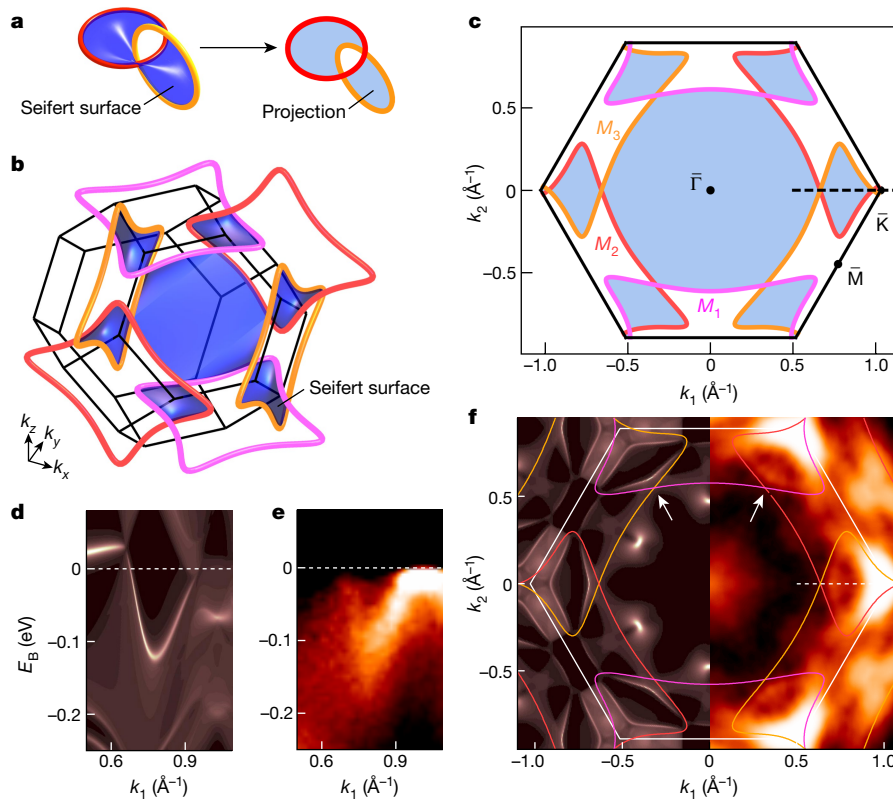
Fig. 5 | Seifert bulk–boundary correspondence. a, A Seifert surface is defined as a three-dimensional surface bounded by a link, shown for the example of a Hopf link. Its two-dimensional projection produces alternating filled and empty regions pinned together at characteristic touching points. **b**, In a condensed-matter system, the Seifert surface is taken as a surface bounded by the linked node loops in three-dimensional momentum space (k_x, k_y, k_z), shown for the case of the link observed in Co_2MnGa. **c**, The projection of the Seifert surface into the (111) surface Brillouin zone is associated with topological boundary modes (blue regions) that touch at points in momentum space. The energy axis is collapsed for clarity. **d**, Ab initio calculation of the surface states

through the touching point, exhibiting pairs of boundary modes pinned together at the Weyl loops. **e**, Surface-sensitive VUV-ARPES energy–momentum cut acquired on the (111) surface Brillouin zone through the loop touching point, exhibiting signatures of the pinned Seifert boundary modes, consistent with ab initio calculations. Photon energy $h\nu = 63$ eV. **f**, Fermi surface in ab initio calculation (left) and VUV-ARPES (right) exhibiting Seifert boundary modes that stretch across the topological regions, connecting different Weyl loops (white arrows), consistent with the Seifert projection. The dashed lines in **c**, **f** indicate the cut shown in **d**, **e**.

composite Weyl loop structure can then be written as (2, 2, 2), in which the first entry in the list corresponds to the linking number between M_1 and M_2, the second entry corresponds to that between M_2 and M_3, and the third entry corresponds to that between M_3 and M_1. By analogy with topological insulators and Weyl point semimetals, this Weyl loop link is expected to be stable under arbitrary, small, symmetry-preserving perturbations of the electronic structure (Extended Data Figs. 9 and 10).

Seifert boundary modes

Having systematically characterized the link structure in the bulk of Co_2MnGa, we next consider its topological surface states. Unlinked loop nodes host conventional drumhead surface states, which typically fill a simply connected region of momentum space in the surface Brillouin zone. By contrast, linked loops exhibit an alternating pattern of topologically distinct regions in which surface states are either present or suppressed, and which are pinned together at generic points in momentum space. This topological structure is captured by the Seifert surface, defined as a three-dimensional surface that has the link as its boundary[28]. For a condensed-matter system, we consider a Seifert surface defined in (k_x, k_y, k_z) and bounded by the linked loop nodes, with the energy axis collapsed. For the minimal case of a Hopf link, the Seifert surface exhibits a branched structure that 'wraps' around the link (Fig. 5a, left). A two-dimensional projection of the Seifert surface then produces alternating filled and empty regions, which meet at

characteristic touching points (Fig. 5a, right). In the case of the Weyl loop link that we observe in Co_2MnGa, the Seifert projection on the (111) hexagonal surface Brillouin zone then predicts several alternating regions with and without topological boundary states (blue and white regions, Fig. 5c), exhibiting touching points along $\bar{\Gamma}–\bar{K}$. As the Seifert surface encodes the linking number[28], the topological boundary states are associated with a Seifert bulk–boundary correspondence. In this correspondence, the linking number of the Weyl loops in the bulk is encoded in a Seifert surface, whose projection gives the topological boundary states. A measurement of the bulk link determines the Seifert boundary states, and a measurement of the Seifert boundary states allows a reconstruction of the bulk linking number.

To explore these possible surface states, we examine the (111) surface of our Co_2MnGa samples in ab initio calculation and surface-sensitive vacuum ultraviolet (VUV) ARPES. On an energy–momentum cut through the touching point, we observe in calculation a pair of surface modes pinned together at the Weyl loops (Fig. 5d). Moreover, our photoemission spectra are consistent with our ab initio prediction, suggesting the observation of Seifert boundary states approaching the Weyl loop linking point (Fig. 5e and Supplementary Section 2). On iso-energy contours of the electronic structure, we expect to observe arc-like slices of the Seifert states, stretching across the filled regions and connecting the linked Weyl loops. Examining the Fermi surface obtained in calculation, we observe a sharp arc of surface states connecting the linked Weyl loops, consistent with the Seifert projection

Article

(Fig. 5f, left, and Supplementary Section 3). At the same time, the suppressed region exhibits no topological surface states in calculation. Our Fermi surface obtained by VUV-ARPES matches the ab initio prediction (Fig. 5f, right). We observe distinct arcs of states connecting the linked Weyl loops across the topological region, corresponding to the topological surface states observed on the energy–momentum cuts (Fig. 5d, e) and suggestive of Seifert boundary modes at the Fermi level in Co_2MnGa.

Conclusion

Our photoemission spectra and theoretical analysis suggest the observation of linked node loops with Seifert bulk–boundary correspondence in a quantum magnet. These results establish a new bridge between physics and knot theory, motivating further exploration of links and knots in electronic structures (Supplementary Sections 4 and 5). Moreover, the linked-loop state in Co_2MnGa, as well as in other materials, may give rise to an exotic response quantized to the linking number, such as a link-quantized topological magneto-electric effect[19,26,27,40]. As magnetic and correlated materials are abundant in a wide variety of symmetry classes, these ideas open the way to the discovery of unusual behaviour in many quantum magnets and superconductors, as well as their photonic analogues[41,42].

Online content

Any methods, additional references, Nature Research reporting summaries, source data, extended data, supplementary information, acknowledgements, peer review information; details of author contributions and competing interests; and statements of data and code availability are available at https://doi.org/10.1038/s41586-022-04512-8.

1. Buchanan, M. The unifying role of topology. *Nat. Phys.* **16**, 818 (2020).
2. Chaikin, P. M. & Lubensky, T. C. *Principles of Condensed Matter Physics* Ch. 9 (Cambridge Univ. Press, 1995).
3. Haldane, F. D. M. Nobel lecture: Topological quantum matter. *Rev. Mod. Phys.* **89**, 040502 (2017).
4. Wen, X.-G. Colloquium: Zoo of quantum-topological phases of matter. *Rev. Mod. Phys.* **89**, 041004 (2017).
5. Volovik, G. E. *The Universe in a Helium Droplet* (Oxford Univ. Press, 2003).
6. Zang, J., Cros, V. & Hoffmann, A. *Topology in Magnetism* (Springer, 2018).
7. Nagaosa, N. & Tokura, Y. Topological properties and dynamics of magnetic skyrmions. *Nat. Nanotechnol.* **8**, 899–911 (2013).
8. Avron, J. E., Osadchy, D. & Seiler, R. A topological look at the quantum Hall effect. *Phys. Today* **56**, 38–42 (2003).
9. Hasan, M. Z. & Kane, C. L. Colloquium: Topological insulators. *Rev. Mod. Phys.* **82**, 3045–3067 (2010).
10. Bernevig, A. *Topological Insulators and Topological Superconductors* (Princeton Univ. Press, 2013).
11. Hasan, M. Z., Xu, S.-Y., Belopolski, I. & Huang, S.-M. Discovery of Weyl fermion semimetals and topological Fermi arc states. *Annu. Rev. Condens. Matter Phys.* **8**, 289–309 (2017).
12. Armitage, N. P., Mele, E. J. & Vishwanath, A. Weyl and Dirac semimetals in three-dimensional solids. *Rev. Mod. Phys.* **90**, 015001 (2018).
13. Chiu, C.-K., Teo, J. C. Y., Schnyder, A. P. & Ryu, S. Classification of topological quantum matter with symmetries. *Rev. Mod. Phys.* **88**, 035005 (2016).
14. Belopolski, I. et al. Discovery of topological Weyl fermion lines and drumhead surface states in a room temperature magnet. *Science* **365**, 1278–1281 (2019).
15. Chang, G. et al. Topological Hopf and chain link semimetal states and their application to Co_2MnGa. *Phys. Rev. Lett.* **119**, 156401 (2017).
16. Wu, Q., Soluyanov, A. A & Bzdušek, T. Non-Abelian band topology in noninteracting metals. *Science* **365**, 1273–1277 (2019).
17. Yan, Z. et al. Nodal-link semimetals. *Phys. Rev. B* **96**, 041103(R) (2017).
18. Ezawa, M. Topological semimetals carrying arbitrary Hopf numbers: Fermi surface topologies of a Hopf link, Solomon's knot, trefoil knot, and other linked nodal varieties. *Phys. Rev. B* **96**, 041202 (2017).
19. Chang, P.-Y. & Yee, C.-H. Weyl-link semimetals. *Phys. Rev. B* **96**, 081114 (2017).
20. Zhong, C. et al. Three-dimensional pentagon carbon with a genesis of emergent fermions. *Nat. Commun.* **8**, 15641 (2017).
21. Bian, G. et al. Topological nodal-line fermions in spin-orbit metal $PbTaSe_2$. *Nat. Commun.* **7**, 10556 (2016).
22. Watanabe, H., Po, H. C. & Vishwanath, A. Structure and topology of band structures in the 1651 magnetic space groups. *Sci. Adv.* **4**, eaat8685 (2018).
23. Wang, Y. & Nandkishore, R. Topological surface superconductivity in doped Weyl loop materials. *Phys. Rev. B* **95**, 060506 (2017).
24. Stenull, O., Kane, C. L. & Lubensky, T. C. Topological phonons and Weyl lines in three dimensions. *Phys. Rev. Lett.* **117**, 068001 (2016).
25. Nandkishore, R. Weyl and Dirac loop superconductors. *Phys. Rev. B* **93**, 020506(R) (2016).
26. Sun, X.-Q., Lian, B. & Zhang, S.-C. Double helix nodal line superconductor. *Phys. Rev. Lett.* **119**, 147001 (2017).
27. Lian, B., Vafa, C., Vafa, F. & Zhang, S.-C. Chern–Simons theory and Wilson loops in the Brillouin zone. *Phys. Rev. B* **95**, 094512 (2017).
28. Seifert, H. Über das Geschlecht von Knoten. *Math. Ann.* **110**, 571–592 (1935).
29. Bergholtz, E. J., Budich, J. C. & Kunt, F. K. Exceptional topology of non-Hermitian systems. *Rev. Mod. Phys.* **93**, 015005 (2021).
30. Li, L., Lee, C. H. & Gong, J. Emergence and full 3D-imaging of nodal boundary Seifert surfaces in 4D topological matter. *Commun. Phys.* **2**, 135 (2019).
31. Carlström, J., Stålhammar, M., Budich, J. C. & Bergholtz, E. J. Knotted non-Hermitian metals. *Phys. Rev. B* **99**, 161115 (2019).
32. Zhang, X. et al. Tidal surface states as fingerprints of non-Hermitian nodal knot metals. *Commun. Phys.* **4**, 47 (2021).
33. Sakai, A. et al. Iron-based binary ferromagnets for transverse thermoelectric conversion. *Nature* **581**, 53–57 (2020).
34. Sakai, A. et al. Giant anomalous Nernst effect and quantum-critical scaling in a ferromagnetic semimetal. *Nat. Phys.* **14**, 1119–1124 (2018).
35. Guin, S. N. et al. Anomalous Nernst effect beyond the magnetization scaling relation in the ferromagnetic Heusler compound Co_2MnGa. *NPG Asia Mater.* **11**, 16 (2019).
36. Park, G.-H. et al. Thickness dependence of the anomalous Nernst effect and the Mott relation of Weyl semimetal Co_2MnGa thin films. *Phys. Rev. B* **101**, 060406 (2020).
37. Markou, A. et al. Hard magnet topological semimetals in xPt_3 compounds with the harmony of Berry curvature. *Commun. Phys.* **4**, 104 (2021).
38. Strocov, V. N. et al. High-resolution soft X-ray beamline ADRESS at the Swiss Light Source for resonant inelastic X-ray scattering and angle-resolved photoelectron spectroscopies. *J. Synchrotron Radiat.* **17**, 631–643 (2010).
39. Strocov, V. N. et al. Soft-X-ray ARPES facility at the ADRESS beamline of the SLS: concepts, technical realisation and scientific applications. *J. Synchrotron Radiat.* **21**, 32–44 (2014).
40. Wu, L. et al. Quantized Faraday and Kerr rotation and axion electrodynamics of a 3D topological insulator. *Science* **354**, 1124–1127 (2016).
41. Zahid Hasan, M. et al. Weyl, Dirac and high-fold chiral fermions in topological quantum matter. *Nat. Rev. Mater.* **6**, 784–803 (2021).
42. Yin, J.-X., Pan, S. H. & Zahid Hasan, M. Probing topological quantum matter with scanning tunnelling microscopy. *Nat. Rev. Phys.* **3**, 249–263 (2021).

Methods

Single-crystal growth

Co$_2$MnGa single crystals were grown using the Bridgman–Stockbarger method. A polycrystalline ingot was first prepared using an induction melt technique, with a stoichiometric mixture of Co, Mn and Ga metal pieces of 99.99% purity. Then the powdered material was poured into an alumina crucible and sealed in a tantalum tube. Growth temperatures were controlled using a thermocouple attached to the bottom of the crucible. During the heating cycle, the material was melted at temperatures above 1,200 °C and then slowly cooled below 900 °C. The conventional unit-cell lattice constant is $c = 5.77$ Å. A representative crystallographic mirror plane is shown in orange in Extended Data Fig. 2a. The corresponding momentum-space mirror planes contain the time-reversal-invariant momentum points X_1, X_2 and X_3, sitting at the centres of the square faces of the bulk Brillouin zone (Extended Data Fig. 2c, d). The structure further exhibits three C_4 rotation symmetries relating any one of these mirror planes to the other two. Without loss of generality, we consider the crystal cleaving plane in our photoemission experiments to be parallel to M_1. We perform a characterization by atomic-level energy-dispersive X-ray spectroscopy (EDS), providing direct structural evidence that our Co$_2$MnGa samples are crystallographically well ordered, show the expected lattice constant and exhibit these mirror and rotation symmetries[43,44] (Fig. 1b).

ARPES

Soft X-ray ARPES measurements were carried out at the ADRESS beamline of the Swiss Light Source in Villigen, Switzerland under a vacuum better than 5×10^{-11} torr and a temperature of 16 K (refs. [38,39,45]). Rod-shaped single crystals of Co$_2$MnGa oriented along the conventional unit-cell $\hat{z}$ direction were cleaved in situ at base temperature. The constant-energy cuts were symmetrized about M_x and M_{xy} (Fig. 1d), M_x and M_{xz} (Fig. 1e) and M_y and M_{yz} (Fig. 1f). The high-symmetry energy–momentum cuts were similarly symmetrized about M_x, M_y or M_z, as appropriate and consistent with the nominal symmetries of the crystal (Fig. 4a). A background was removed from the photoemission spectra by a fixed intensity cutoff (raw, unsymmetrized data in Extended Data Figs. 6–8). For the Fermi surfaces acquired at $h\nu = 544$ eV, the nominal energy resolution was $\delta E = 75$ meV; for the photon-energy dependences, the nominal energy resolution varied from $\delta E = 75$ meV at $h\nu = 500$ eV to $\delta E = 125$ meV at $h\nu = 800$ eV. The angular resolution was better than 0.2° in all cases. The Fermi surfaces were binned in an energy window of ± 38 meV (Fig. 1d) and ± 25 meV (Fig. 1e, f) around E_F. VUV-ARPES measurements were carried out at Beamline 5-2 of the Stanford Synchrotron Radiation Lightsource in Menlo Park, CA, USA at $\delta E = 15$ meV and temperature 20 K. The inner potential for converting $h\nu$ to k_z was determined to be $V_0 = 22$ eV.

Ab initio calculations

The electronic structure of Co$_2$MnGa in the ferromagnetic phase was calculated within the density functional theory (DFT) framework using the projector augmented-wave method as implemented in the VASP package[46,47]. The generalized gradient approximation (GGA)[48] and a Γ-centred k-point $12 \times 12 \times 12$ mesh were used. Ga s and p orbitals and Mn and Co d orbitals were used to generate a real-space tight-binding model, from which Wannier functions were determined. The Fermi level in DFT was shifted to match the ARPES.

Scanning transmission electron microscopy

Thin lamellae for microstructure characterization were prepared from bulk single crystals by focused ion beam cutting using a Helios NanoLab G3 UC dual-beam focused ion beam and scanning electron microscope (FIB/SEM) system. Atomic-resolution high-angle annular dark-field (HAADF) scanning transmission electron microscopy (STEM) imaging and atomic-level energy-dispersive X-ray spectroscopy (EDS) mapping were performed on a double Cs-corrected Titan Cubed Themis 300 scanning/transmission electron microscope (S/TEM) equipped with an X-FEG source operated at 300 kV with a Super-X EDS system.

Weyl loop trajectory from SX-ARPES

We fit the Weyl cone crossing points to a two-band effective $\mathbf{k} \cdot \mathbf{p}$ Hamiltonian for a Weyl loop

$$H = \sum_{k,\ a,b\in\{\pm\}} c^\dagger_{ka} h_{ab}(k) c_{kb}, \quad h(k) = f(k)\sigma_z + v_F q_z \sigma_x + g(k)\mathbb{1} \tag{1}$$

Here the $c^\dagger_{ka}$ terms are fermionic creation operators, k is the crystal momentum, σ_z and σ_x are Pauli matrices, $\mathbb{1}$ is the 2×2 identity and $q_z \equiv k_z - 2\pi/c$ is the $\hat{z}$ component of the momentum measured relative to M_1, in which c is the conventional unit-cell lattice constant. This Hamiltonian exhibits a Weyl loop on $q_z = 0$ with a trajectory given by $f(k) = 0$, formed from two bands with opposite mirror eigenvalues. From our ARPES spectra, we experimentally extract the full Weyl loop trajectory by fitting to a low-order expansion around X_1, consistent with the symmetries of the system

$$f(k) = \gamma\left(1 + \alpha\left(k_x^2 + k_y^2\right) + \beta k_x^2 k_y^2\right) \tag{2}$$

Here α and β fix the Weyl loop trajectory and the scaling factor γ sets an energy scale. The train of crossing points observed in ARPES is well captured by $\alpha = -1.23 \pm 0.03$ Å^2 and $\beta = -31.5 \pm 4.1$ Å^4 (Fig. 2c). We also find that our ARPES-extracted Weyl loop trajectory agrees well with the trajectory observed in ab initio calculations (Extended Data Fig. 3). The energy dispersion of the Weyl loop is set by $g(k)$, well described by $g(k) = \delta + \eta\cos(4\theta)$, in which $\delta = -75 \pm 17$ meV, $\eta = 46 \pm 17$ meV and θ is the ordinary polar angle of k, $\tan\theta \equiv k_y/k_x$. Away from the loop, the bands disperse linearly. We observe that the experimental dispersion is well captured by $\gamma = 0.15 \pm 0.05$ eV. Our analytical model, with all parameters extracted from photoemission spectra, allows us to achieve a complete experimental characterization of both the momentum trajectory and energy dispersion of the family of Weyl loops (Fig. 2e and Extended Data Fig. 3)[49].

Stability of the linked node loops

To estimate the stability of the link, we can measure how far apart one would need to slide two Weyl loops to unlink them (Extended Data Figs. 4 and 5). From the loop Fermi surfaces, we find that the typical 'depth' of the link in momentum space is $d_{avg} = 0.58 \pm 0.08$ Å^{-1}, of the same order of magnitude as the radius $|k|_{avg}$ of the Weyl loop. This large depth suggests that the system lives well within a linked electronic phase.

Data availability

The datasets generated during and/or analysed during the current study are available in the Zenodo repository at https://doi.org/10.5281/zenodo.5793667. Source data are provided with this paper.

43. Webster, P. J. Magnetic and chemical order in Heusler alloys containing cobalt and manganese. *J. Phys. Chem. Solids* **32**, 1221–1231 (1971).
44. Ido, H. & Yasuda, S. Magnetic properties of Co-Heusler and related mixed alloys. *J. Phys.* **49**, C8-141–C8-142 (1988).
45. Strocov, V. N. et al. Three-dimensional electron realm in VSe$_2$ by soft-X-ray photoelectron spectroscopy: origin of charge-density waves. *Phys. Rev. Lett.* **109**, 086401 (2012).
46. Kresse, G. & Furthmueller, J. Efficient iterative schemes for *ab initio* total-energy calculations using a plane-wave basis set. *Phys. Rev. B* **54**, 11169–11186 (1996).
47. Kresse, G. & Joubert, D. From ultrasoft pseudopotentials to the projector augmented-wave method. *Phys. Rev. B* **59**, 1758–1775 (1999).
48. Perdew, J. P., Burke, K. & Ernzerhof, M. Generalized gradient approximation made simple. *Phys. Rev. Lett.* **77**, 3865–3868 (1996).
49. Belopolski, I. et al. Signatures of Weyl fermion annihilation in a correlated kagome magnet. *Phys. Rev. Lett.* **127**, 256403 (2021).
50. Salomaa, M. M. & Volovik, G. E. Quantized vortices in superfluid ^{3}He. *Rev. Mod. Phys.* **59**, 533–613 (1987).

Article

51. Nakahara, M. *Geometry, Topology and Physics* (Institute of Physics, 2003).
52. Bansil, A., Lin, H. & Das, T. Colloquium: Topological band theory. *Rev. Mod. Phys.* **88**, 021004 (2016).
53. Kane, C. L. in *Topological Insulators* Ch. 1 (Elsevier, 2013).
54. Tokura, Y., Yasuda, K. & Tsukazaki, A. Magnetic topological insulators. *Nat. Rev. Phys.* **1**, 126–143 (2019).
55. Hasan, M. Z., Xu, S.-Y. & Bian, G. Topological insulators, topological superconductors and Weyl fermion semimetals: discoveries, perspectives and outlooks. *Phys. Scr.* **2015**, T164 (2015).
56. Yin, J.-X. et al. Quantum-limit Chern topological magnetism in TbMn$_6$Sn$_6$. *Nature* **583**, 533–536 (2020).
57. Chen, W., Lu, H.-Z. & Hou, J.-M. Topological semimetals with a double-helix nodal link. *Phys. Rev. B* **96**, 041102 (2017).
58. Muro, T. et al. Soft X-ray ARPES for three-dimensional crystals in the micrometre region. *J. Synchr. Radiat.* **28**, 1631–1638 (2021).
59. Strocov, V. N. et al. Soft-X-ray ARPES at the Swiss Light Source: from 3D materials to buried interfaces and impurities. *Synchrotron Radiat. News* **27**, 31–40 (2014).

Author contributions M.Z.H. supervised the project. I.B., G. Chang and T.A.C. initiated the project. I.B., T.A.C., Z.-J.C. and M.Z.H. acquired and analysed ARPES spectra with help from X.P.Y., D.M., J.-X.Y., M. Litskevich, N.S. and S.S.Z. ARPES measurements were supported by N.B.M.S., A.C., C.P., B.T., M. Leandersson, J.A. and V.N.S. G. Chang performed the first-principles calculations. I.B. wrote down the $\mathbf{k} \cdot \mathbf{p}$ model with help from G. Chang and S.-M.H. I.B. developed the linking number theory with help from C.H. G. Cheng and N.Y. performed the scanning transmission electron microscopy measurements. K.M., C.S. and C.F. synthesized and characterized the single crystals. I.B. wrote the manuscript with contributions from all authors.

a Magnetic vortex

b Topological insulator

c Linked node loops
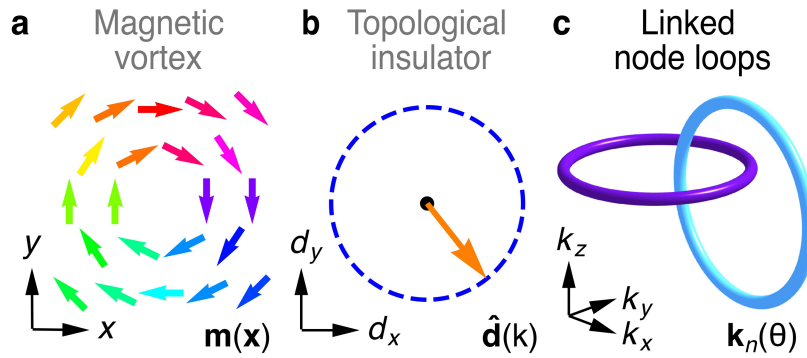
Extended Data Fig. 1 | Topological invariants in physics. a, An example of an order parameter winding in real space: a magnetic vortex[2,5–7,50,51]. In this case, the order parameter is the local magnetization $m(\mathbf{x})$, confined to a magnetic easy plane in real space (x, y). It may happen that $m(\mathbf{x})$ winds around a point in real space, forming a magnetic vortex characterized by a winding number topological invariant, in this example given by $w = 1$. **b**, An example of a quantum wavefunction winding in momentum space: the one-dimensional topological insulator (Su-Schrieffer-Heeger model)[3,4,8–13,52–56]. This phase is described by Bloch Hamiltonian $h(k) = \mathbf{d}(k) \cdot \sigma$, where k is the one-dimensional crystal momentum, σ refers to the Pauli matrices and $\mathbf{d}(k)$ is a two-component object confined to the (d_x, d_y) plane. The normalized quantity $\widehat{\mathbf{d}}(k) \equiv \mathbf{d}(k)/|\mathbf{d}(k)|$ (orange arrow) moves around the unit circle (dotted blue) as k varies. The topological invariant is related to how many times $\widehat{\mathbf{d}}(k)$ winds around the origin as k scans through the one-dimensional Brillouin zone. **c**, Node loops linking in momentum space[17–20,57]: a three-dimensional electronic structure may exhibit multiple node loops (cyan and purple), characterized by $\mathbf{k}_n(\theta)$, where n indexes the loops and θ parametrizes the loop trajectory in momentum space. The loops may link one another, encoding a linking number topological invariant. This example shows a Hopf link. (See also Supplementary Information.).
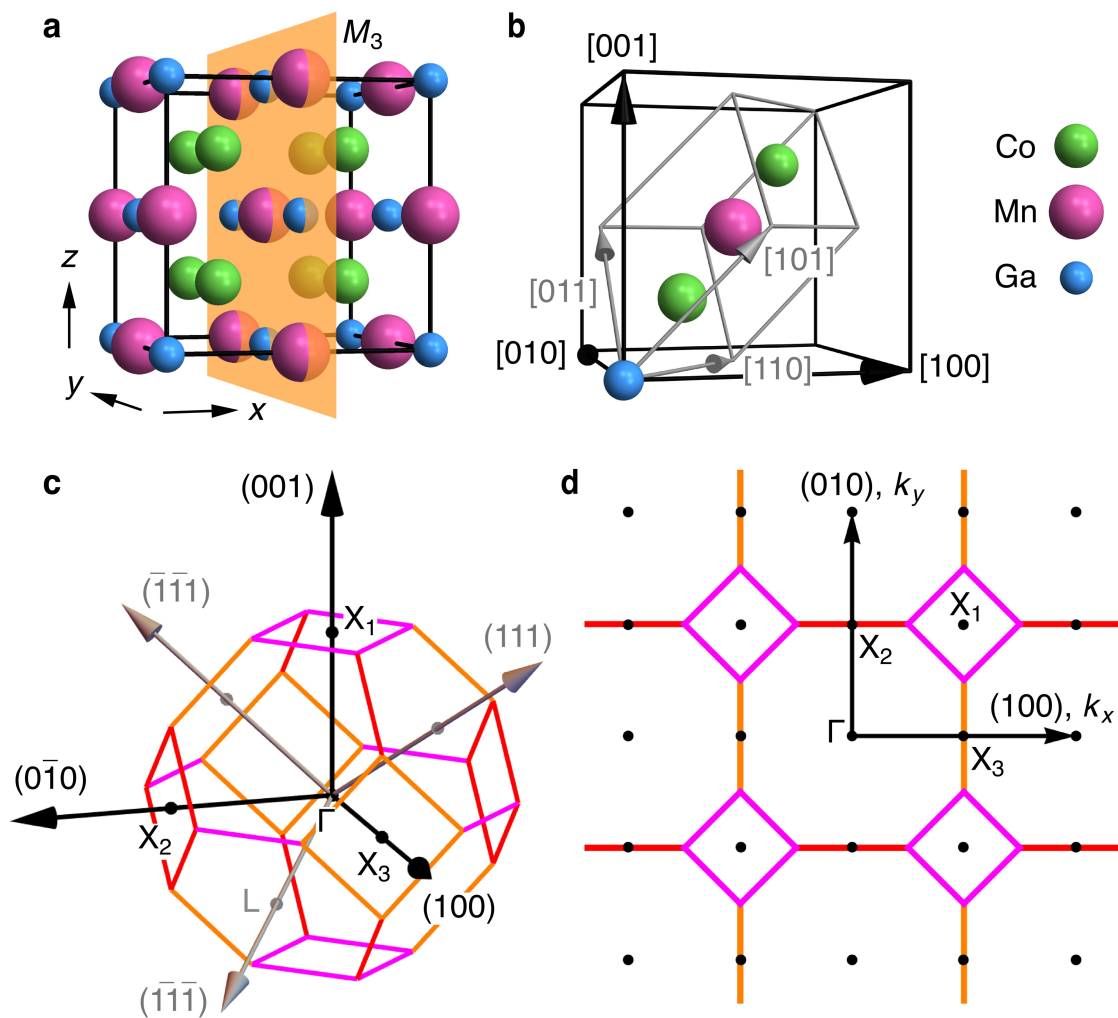
Extended Data Fig. 2 | Crystal structure and Brillouin zone of Co₂MnGa.
a, Conventional unit cell with representative crystallographic mirror plane M (orange). **b**, The primitive unit cell (grey) includes one formula unit. **c**, Brillouin zone, with conventional reciprocal lattice basis vectors (black). Brillouin zone edges color-coded to correspond to the mirror planes: magenta M_1 plane, (001); red M_2 plane, (010), orange M_3 plane, (100). **d**, Slice through Γ in an extended zone scheme.
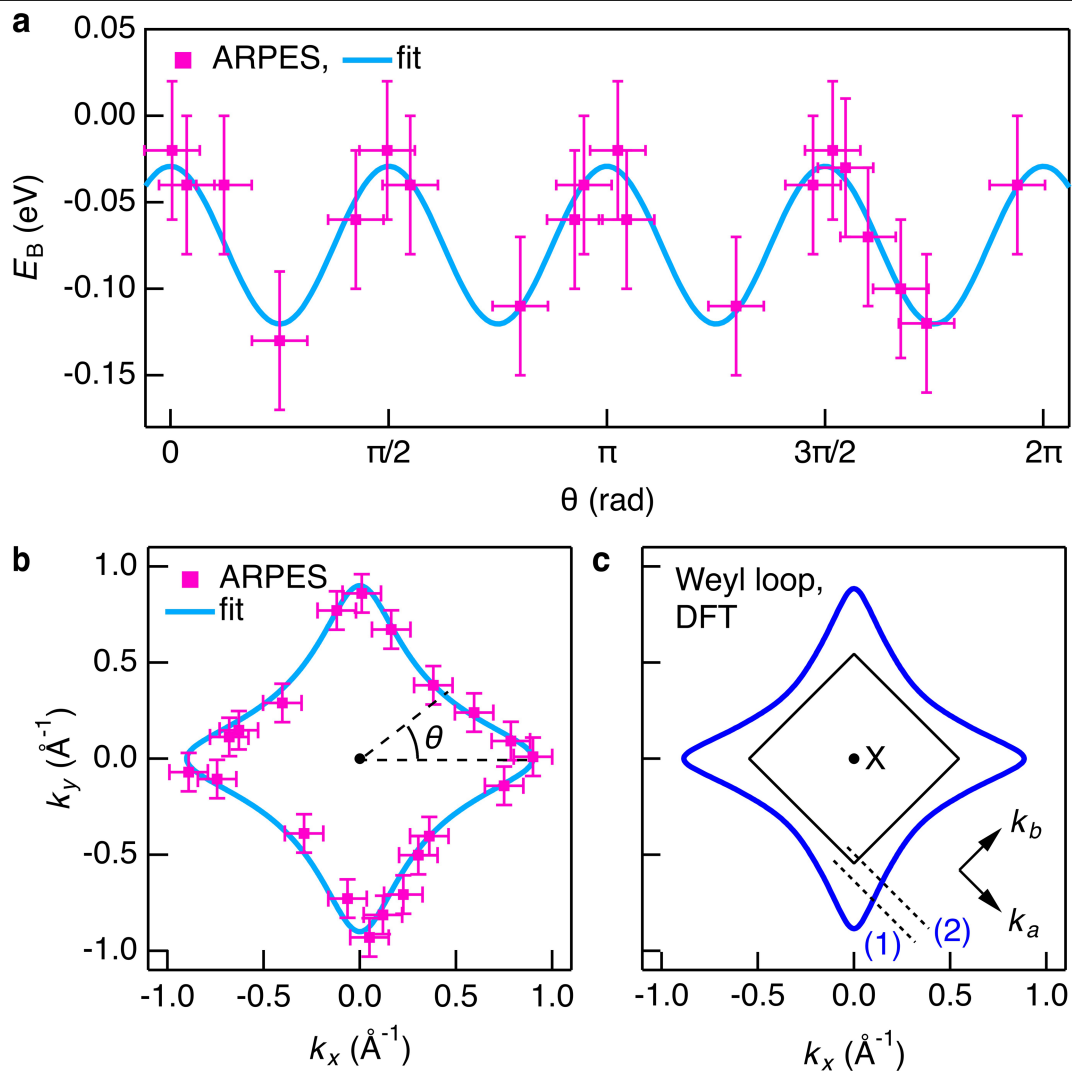
Extended Data Fig. 3 | Energy dispersion of the Weyl loop. a, Crossing point energies E_B and **b**, crossing point momenta (k_x, k_y) systematically extracted from cone dispersions observed in the ARPES spectra (magenta squares), same dataset as Fig. 2c ($hv = 544$ eV), with fit of the Weyl loop momentum trajectory and energy dispersion (cyan, see main text). The crossing point energies are parametrized by a polar angle θ defined by $\tan \theta \equiv k_y/k_x$. **c**, Weyl loop trajectory from DFT, with dotted lines indicating the DFT energy-momentum slices shown in Fig. 2b. The binding energy axes in (b) and (c) are collapsed[58].
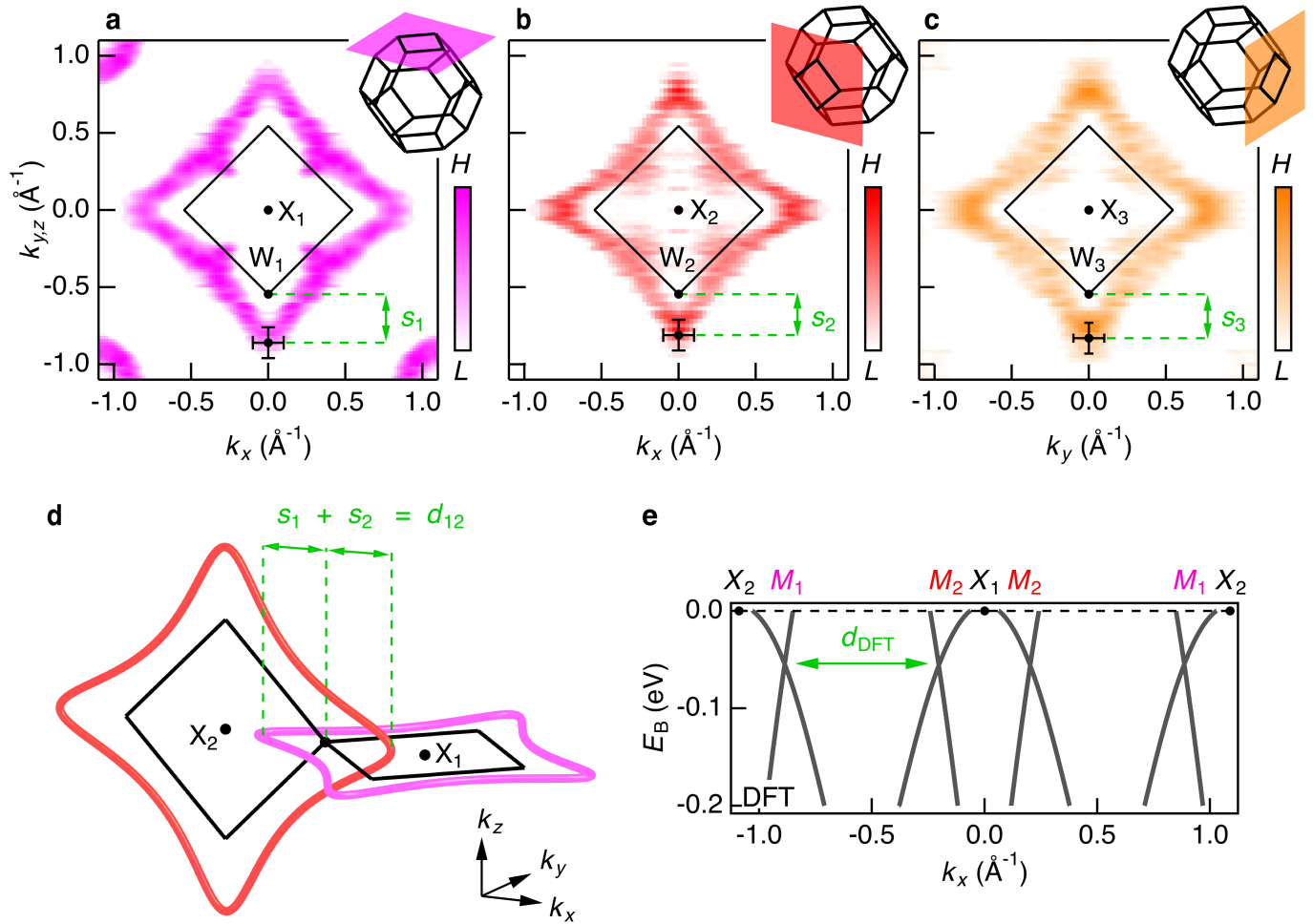
Extended Data Fig. 4 | Link 'depth' of the Weyl loops. a–c, Distance between the extrema of the Weyl loops and the bulk Brillouin zone W points for the M_1, M_2 and M_3 Weyl loops. We estimate $s_1 = 0.32 \pm 0.1\,\text{Å}^{-1}$, $s_2 = 0.27 \pm 0.1\,\text{Å}^{-1}$ and $s_3 = 0.29 \pm 0.1\,\text{Å}^{-1}$. **d,** The link depth captures how far in momentum space one would need to slide the Weyl loops in order to unlink them, providing a measure of the stability of the link. Based on the loop Fermi surfaces (**a–c**), we estimate $d_{12} = 0.58 \pm 0.14\,\text{Å}^{-1}$, $d_{23} = 0.55 \pm 0.14\,\text{Å}^{-1}$ and $d_{31} = 0.60 \pm 0.14\,\text{Å}^{-1}$. The average gives a typical link depth extracted from ARPES, $d_{avg} = 0.58 \pm 0.08\,\text{Å}^{-1}$. **e,** Energy-momentum slice along the high-symmetry path $X_1 - X_2$ from DFT, passing through two linked Weyl loops. We obtain $d_{DFT} = 0.68\,\text{Å}^{-1}$.
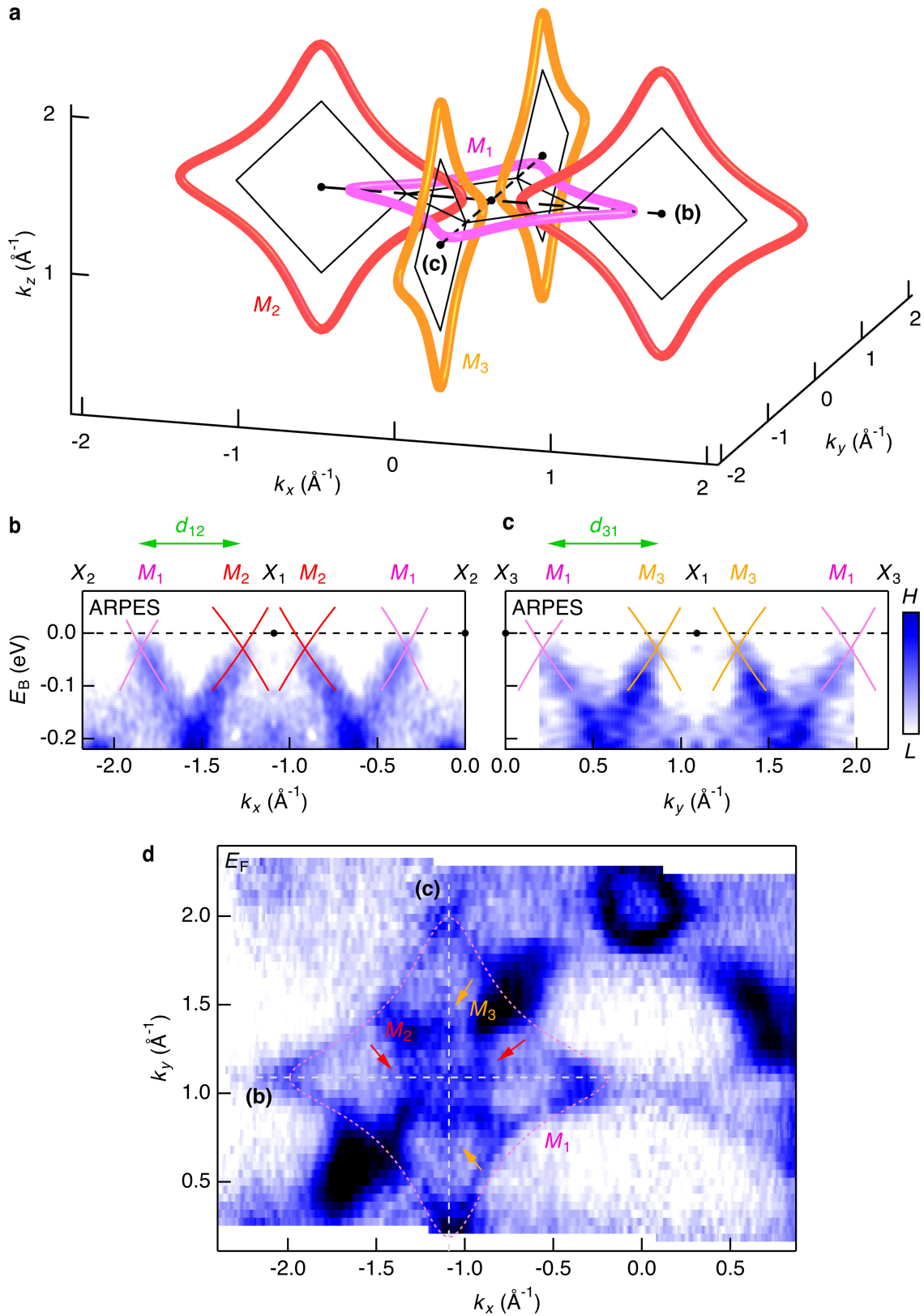
Extended Data Fig. 5 | Supplementary measurement of the link depth. a, M_1, M_2 and M_3 Weyl loops, with trajectories obtained from the analytical model (see main text), showing that M_1 links M_2 twice and M_3 twice. Energy-momentum photoemission cuts along the high-symmetry paths **b**, $X_1 - X_2$ and **c**, $X_3 - X_1$ obtained at photon energy $h\nu = 642$ eV. We observe $d_{12} = 0.56 \pm 0.1$ Å^{-1} and $d_{31} = 0.61 \pm 0.1$ Å^{-1}, consistent with Extended Data Fig. 4. For both cuts, exactly one branch of each Weyl cone exhibits appreciable photoemission cross-section, as expected from the mirror-symmetric measurement geometry[59]. **d**, Fermi surface acquired at $h\nu = 642$ eV, exhibiting an in-plane Weyl loop contour, M_1. We further observe spectral weight emanating along k_x and k_y from the center of M_1, corresponding to the linearly dispersive branches in (**b**, **c**), again suggesting that M_1 is linked by M_2 and M_3.
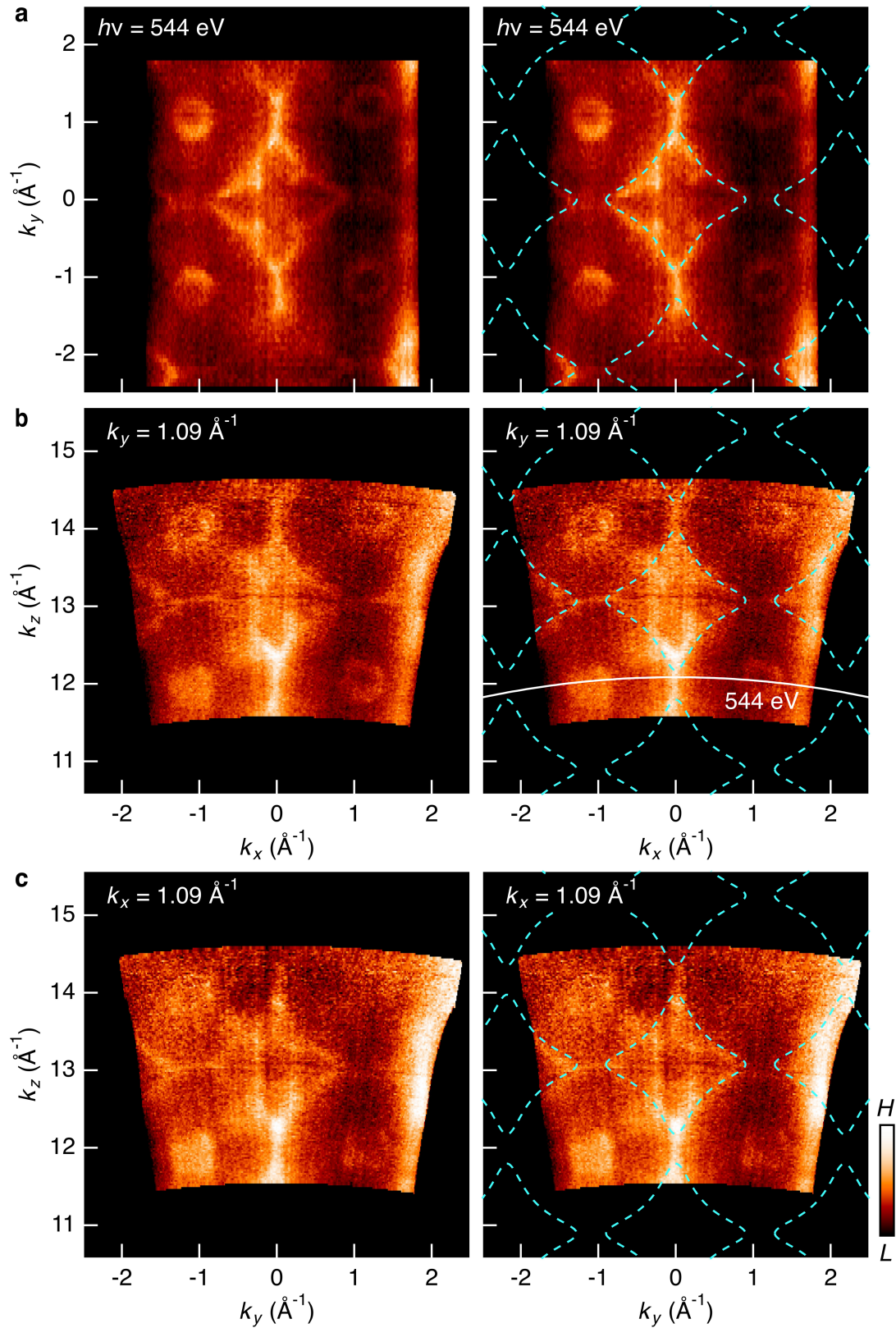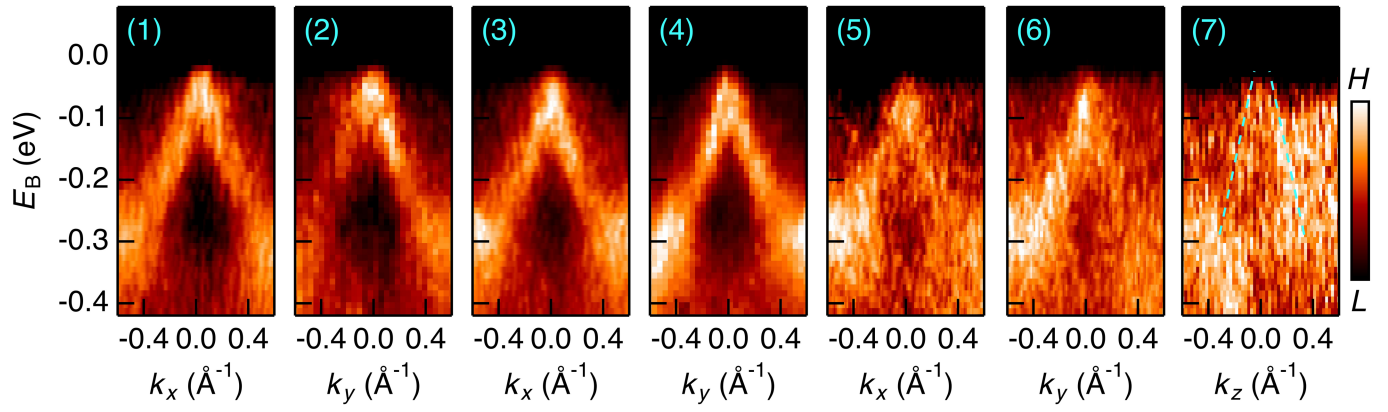
Extended Data Fig. 6 | Unsymmetrized Fermi surfaces. a–c, Left: photoemission spectra displayed in Fig. 1d–f, without symmetrization. Right: the same spectra, with the experimentally-determined Weyl loop trajectory overlaid across multiple Brillouin zones. The irrelevant Γ pocket is consistently observed in all unsymmetrized spectra. Signatures of Weyl loops are observed around all X points.
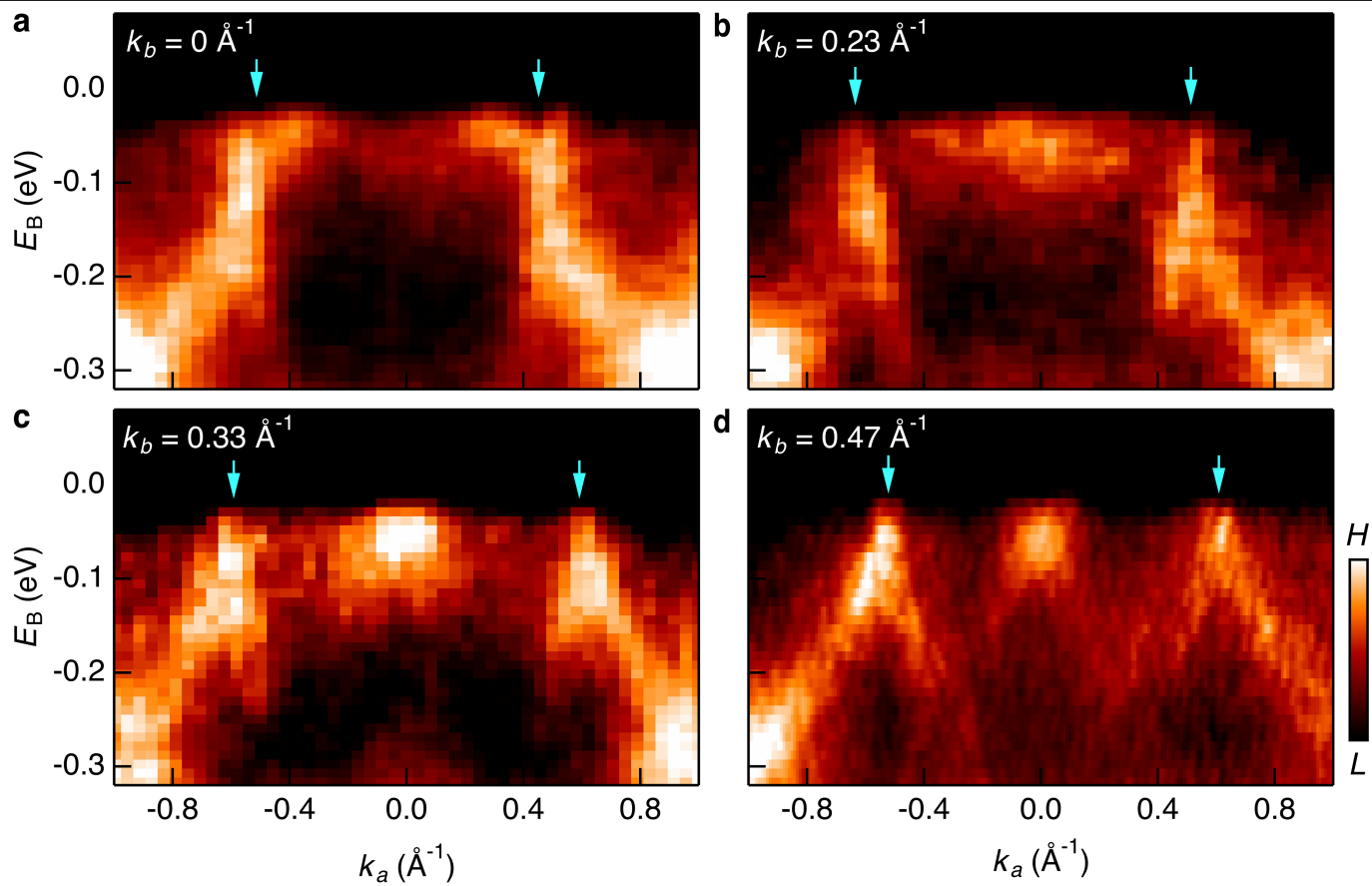
Extended Data Fig. 7 | SX-ARPES systematics. a–d, Photoemission energy-momentum cuts through the Weyl loop, used to extract Fig. 2c.

Extended Data Fig. 8 | Unsymmetrized energy-momentum cuts. Photoemission spectra displayed in Fig. 4a, without symmetrization.

a

X_3

X_1

k_z

k_y

k_x

b

X_1

X_2

X_3
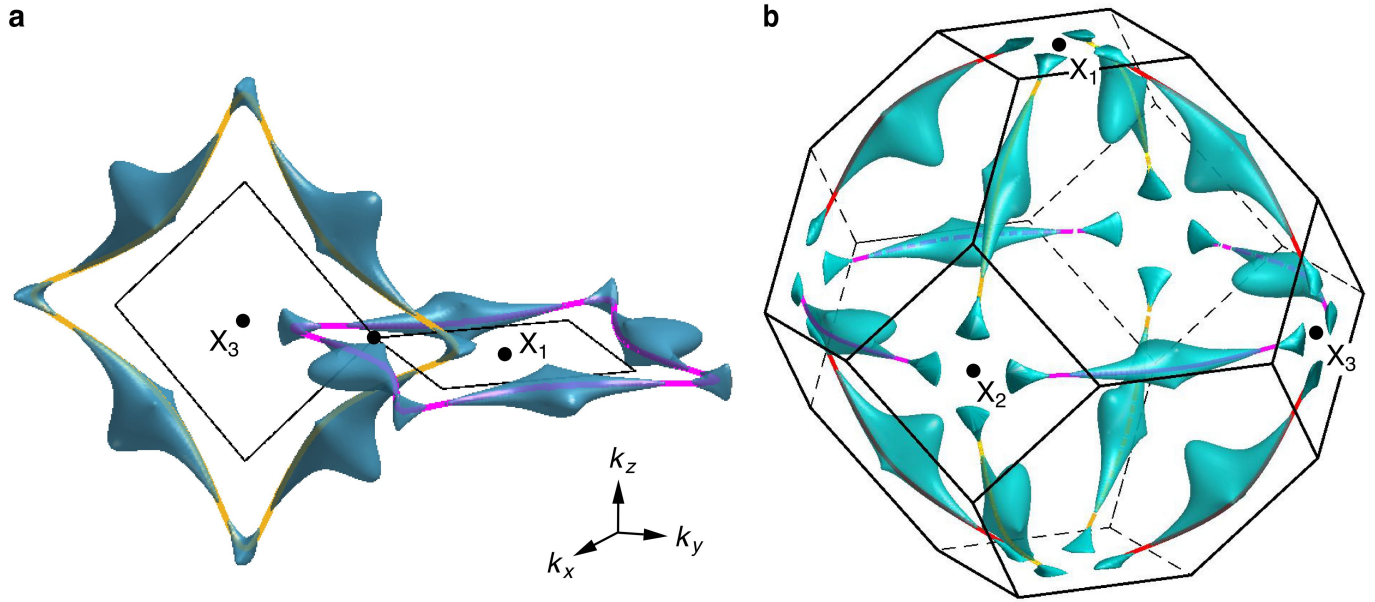
Extended Data Fig. 9 | Linked Weyl loop Fermi surface. Constant-energy slice of the pockets (navy) making up the linked Weyl loops obtained by *ab initio* calculation, at binding energy $E_B = -10$ meV below the experimental Fermi level. Plotted **a**, in an extended zone scheme (only two loops shown for simplicity) and **b**, the reduced Brillouin zone (all three loops shown). The Fermi surface pockets touch at a set of discrete points, where the Weyl loop disperses through this particular E_B. For reference, the full Weyl loop trajectories are indicated, collapsed in energy (magenta around X_1, red around X_2, orange around X_3). The Weyl loop Fermi surface pockets form a linked structure.
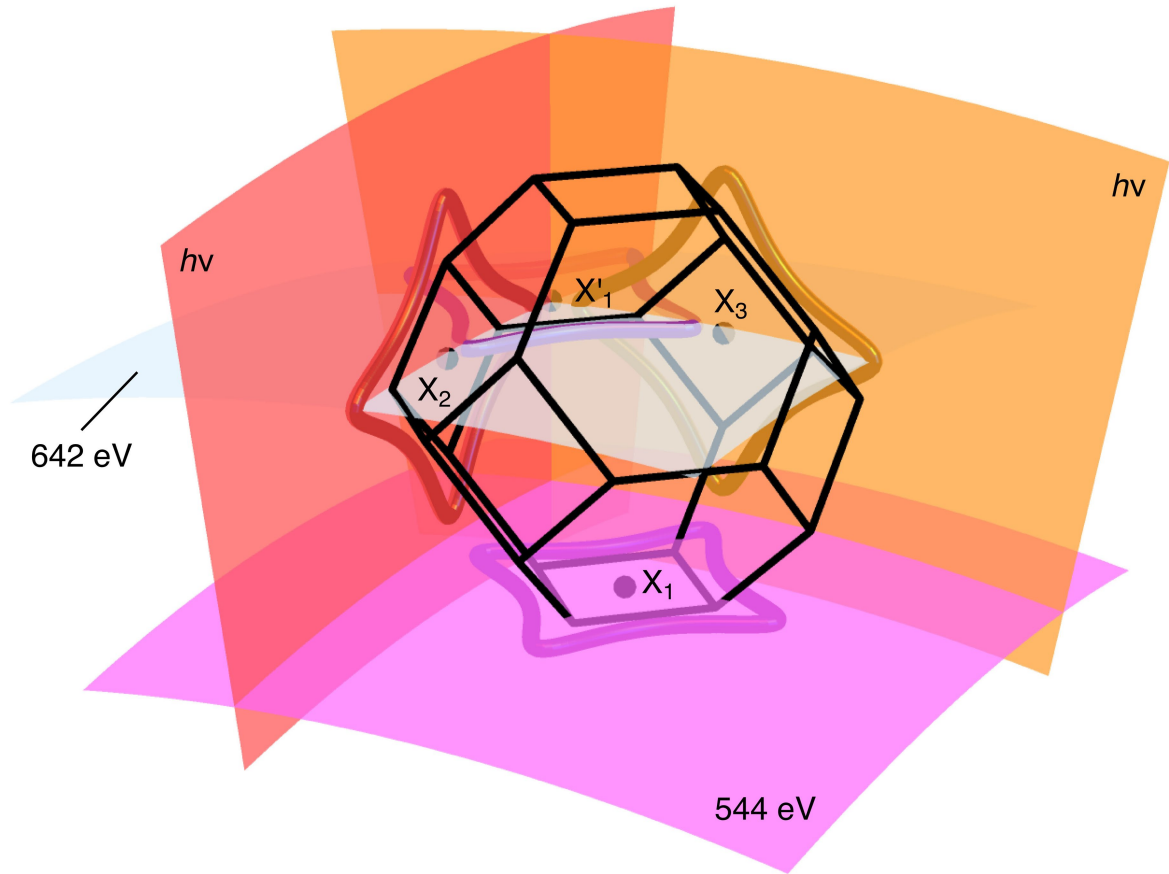
Extended Data Fig. 10 | Measured Fermi surfaces in an extended zone scheme. The Brillouin zone corresponds to $\Gamma_{(066)}$ in the primitive reciprocal basis.